Title: Tracing immune cell around biomaterials with spatial anchor during wound regeneration

Authors: Yang Yang[1]†, Chen-yu Chu[1]†, Li Liu[1], Chen-bing Wang[1], Chen Hu[1], Xin-hui Li[1], Yi-li Qu[1]*, Yi Man[1]*

Affiliations:

[1] Department of Oral Implantology &State Key Laboratory of Oral Diseases & National Clinical Research Center for Oral Diseases, West China Hospital of Stomatology, Sichuan University; Chengdu 610041, China.

* Corresponding author. Email: manyi780203@126.com (Y.M.); qqyili@126.com (Y.L.Q.)

† These authors contributed equally to this work

Abstract: Generally, only few hair follicle can regenerate upon severe wound in adult mammals, which restricted in the large wound center, termed wound-induced hair follicle neogenesis. We observed the enhanced WIHN with the implantation of extracellular matrix scaffold regardless of wound size. The paired analysis of single-cell RNA with spatial resolution during wound regeneration provided a unique lens through which we can explored delicate cellular interactions. The spatial anchor highlighted the preferential aggregation of adaptive immune cells in large wound center co-localizing with HF precursor cells. Recruited adaptive immune cells surrounding biomaterials might exerted further pro-regenerative effect on HF neogenesis. Immunodeficient mice lacking mature adaptive immune cells lost the ability to stimulate WIHN, which validated the potential therapeutic effect of adaptive immune system in appendages regeneration.

One-Sentence Summary: Multimodal analysis tracing the regenerative effect of adaptive immune system activated by biomaterial during wound healing

Main Text:

Extracellular matrix (ECM) scaffolds are one of the efficient treatments for severe wound (*1*) but still lacking ability of stimulating hair follicle (HF) neogenesis(*2*). Intriguingly, rare capacity of HF regeneration has been observed in large full-thickness wound center in wound-induced hair follicle neogenesis (WIHN) model(*3, 4*). It has been suggested that immune cells (mainly

macrophages, T cells) might be the key orchestrators of wound healing that selectively promoting scarring(*5-7*) or regenerative WIHN(*8-11*), while the spatial heterogeneity of immune systems still unclear. Biological cues can be integrated into polymer scaffold to create a mimic of the native ECM, which is the framework guiding the activity of immune cells (*12, 13*). Our previous study has showed that the ECM scaffold was able to lead to an enhanced regeneration of HF along with the immunomodulatory effect (*14, 15*). However, the spatial distribution of immune cells under single cell RNA transcriptome level remains unclear. Firstly, circular splinted excisional wound healing model was employed to evaluate the relationship between wound size and HF regeneration. We found the diameter 1.5cm was the critical threshold to stimulate WIHN, marked by de novo HF regeneration restricted in wound center. Next we noticed that the ECM scaffold exerts the further pro-regenerative effect on enhancing de novo HF regeneration. Multiomic approaches including spatial transcriptomic (scRNA-seq) and spatial transcriptomic (ST) were applied to trace the cell heterogeneity on the area we interested. Unrevealing the immune cell composition around biomaterials provided the further understanding of foreign body response (FBR) and anchored the key role of adaptive immune cell in HF regeneration. Finally, we observed that immunodeficient mice lacking mature T lymphocyte and macrophages were unable to stimulate HF regeneration, which confirmed that the adaptive immune system activated by biomaterials was crucial in scar-less wound healing.

WIHN model construction

We created circular wound with different diameter in murine splinted full-thickness excisional wound healing model (Fig. 1A and B). By comparison the de novo HF number, we confirmed the threshold value (diameter = 1.5cm) of triggering WIHN phenomenon (Fig. 1C). To explore the underlying mechanism, we respectively created small wound (diameter = 0.6cm) as Ctrl_SW group, and large wound (diameter = 1.5cm) as Ctrl_LW group. Wound tissue was harvested for the further examination (Fig. 1D). Based on bulk-tissue RNA sequencing (bulk-seq) profile, we observed that the large wound showed up-regulated gene expression enriched in hair follicle development and αβT cell differentiation (Fig. 1E). Correlation heatmap also showed the positive correlation between HF regeneration related genes and adaptive immune response related genes (Fig. 1 F). Immunofluorescent (IF) staining (Fig. 1G) and flow cytometry (Fig. 1H) confirmed that large wound (especially wound center) maintained substantial adaptive T cell infiltration.

Tracing the distribution of single cells in WIHN model

To explore the spatial characteristic of single cells during wound healing, we applied the ST and scRNA-seq to compare spatial gene expression profiles between small and large wound (Fig. 2A). The single cell annotation process was showed in Supplementary Text in Supplementary Materials (fig. S1-S4). We observed higher proportion of HF precursor cells including hair follicle progenitor (HFP) (*16*) , hair follicle stem cell (HFSC) (*8*) and papillary fibroblast (PF) (*17, 18*) from Ctrl_LW group (fig.S2 A and G). Based on ST profile, the anatomical structure of the wounds could be clearly distinguished (Fig. 2B). Scoring spots in each section with marker genes from scRNA-seq showed that the PF (HF-related) exhibit strong spatial preferences within the large wound center (Fig. 2D), which might account for the subsequent HF regeneration. In contrast, reticular fibroblast (RF) and lipo fibroblast (LF) in relation to collagen deposition were the dominant subtypes driving small wound healing (Fig. 2E), which might explain the reason why small wound generally heal with scarring devoid of HF. Gene enrichment analysis showed that the Ctrl_LW sample up-regulated genes related to hair follicle morphogenesis as well as antigen presentation (Fig. 2C). Subclustering analysis of ST showed that those genes preferentially expressed in large wound center (fig. S5~S6).To explore how distinct immune cell types may contribute to the regeneration process, the heterogeneity of immune cell subclusters were evaluated next (fig. S3~S4). As shown in Fig. 2F, monocyte (Mono), pro-inflammatory macrophage (PIM), and anti-inflammatory macrophage (AIM) diffusely distributed in small wounds, while Mono (related to antigen presentation) and PIM (related to pro-inflammatory pathways) showed the preferentially aggregation in large wound center. Besides, the Ctrl_LW group showed the higher proportion of adaptive T cells (Fig. 2I). Almost all T cell subclusters were exclusively expressed in large wound center (Fig. 2H). In contrast, there seem lack observable T cell infiltration in small wound. To sum up, it was in large wound that we observed the preferential aggregation of PF (HF-related) as well as adaptive T cells, Mono and PIM, which laid the foundation the potential cellular communication among them.

Cellular communication landscape between immune cell and HF-related cutaneous cell

Next, to address potential interactions between defined cell subclusters (fig. S2~S4), especially co-localized subpopulations including PF and adaptive immune cells (fig. S7A) .Cell Chat(*19*) was applied to predict the cell-cell communication patterns at the level of ligand/receptor expression (fig. S7B). By comparing the interaction strength (information flow), we could identify signaling pathways decrease (turn-off) or increase (turn-on) in different biologic

conditions. We selected up-regulated pathways and compared the overall signaling strength of ligand-receptors that exhibit different signaling patterns (fig. S7C). Adaptive immune system related pathways including MHC-I, MHC-II and CD80 was exclusively enriched in large wound. The major signaling among immune cell and cutaneous cell in large wound was mediated by PF (HF-related). As shown in fig. S7D, adaptive immune cells and hair follicle precursor cells were enriched for interacting ligand or receptor gene partners such as Il6/Il6st, Inhba/Acvr1b. Spatial plots showed the preferentially aggregation of Il6 and Inhba in large wound. The essential role of activin(*20, 21*) and Il6(*10*) pathway in HF regeneration has been reported. Our result suggested that immune cell especially T cells, Mono and PIM may modulate the states of PF, Hair follicle progenitor (HFP) and Hair follicle stem cell (HFSC) through signaling pathways such as IL-6 and activin.

Enhanced WIHN occurred in scaffold-implanted wound with the further activation of adaptive immune system

Synthetic graft transplantation is one of the efficient treatments for severe large area wound of skin especially when patient's donor site is not qualified(*1*). With the further understanding of tissue engineering, it is suggested that synthetic biomaterials imitating the native structure of native ECM structure can integrate and play potentially pro-regeneration role to wound healing(*12, 22*). Our previous report has illustrated the immuno-regulatory effect of ECM scaffold in small wound (diameter=0.6cm) healing(*14, 15*). We next repeated large full-thickness wound-healing model in C57BL/6 mice with/without implanted biomaterial to investigate if the further regenerative phenomenon observed in ECM scaffold treated wounds. Workflow for evaluating large wound healing was summarized in Fig. 3A. We placed ECM scaffolds below the large wound (diameter,1.5 cm; Fig. 3B) in ECM_LW group, while the Ctrl_LW group received no materials. Wound coverage was faster in the ECM_LW group (Fig. 3, C and D), and the ECM_LW also had the smaller gap width (Fig. 3, E and G). IF staining for cytokeratin 5 (Krt5) and cytokeratin 10 (Krt10) showed that keratinocyte crawling around the biomaterials (Fig. 4I), and the ECM_LW group had the larger area of neo-epithelium (Fig. 3J). As showed in Fig. 4F, the ECM membrane implanted in large wound did not trigger an obvious fibrous capsule and owned a rapid degradation rate in vivo. We could observe the degrading fragments on POD 14 and degrading particles on POD21, and there were not any visible remaining on POD28 (Fig. 3F). In addition, the outline of HF morphogenesis could be recognized in ECM_LW group: with the first appearance in hair germ stage on POD7, they gradually grew into bulbous-peg structure

overlaid the degrading scaffold fragments on POD21. On POD28, we found that ECM_LW group recapitulated normal skin architecture with equivalent number of mature appendages and "basket-wave" ECM collagen deposition (Fig. 3H). In summary, in mice large full-thickness wound model, the biomaterial led to the faster wound healing and enhanced regeneration of HF. The excellent biocompatibility and degradability of membrane also avoid the risk of immune rejection and secondary surgery in further clinical applications. To explore the underlying mechanism, we noticed the ECM_LW group showed increased enrichment of genes involved in the hair follicle development as well as T cell differentiation (Fig. 3K). IHC staining and flow cytometry confirmed the increased T cell infiltration around implanted biomaterials (Fig. 3J).

Discovery the spatial heterogeneity around biomaterials at single cell resolution

To explore the spatial characteristic of cell heterogeneity in scaffold-implanted wound, we also applied the ST and scRNA-seq to analyze spatial gene expression profile(Fig. 4A). The anatomical structure could also be identified in ST sections (Fig. 4B). Based on scRNA-seq analysis, the ECM_LW group owned the higher proportion of HF precursor cells (Fig.4 E). Spatial feature plot illustrated the keratinocyte crawling around implanted biomaterials (Fig. 4 D). What's more, we observed that the distribution of PF (HF-related) was enlarged in ECM_LW group. In contrast, lower lineage fibroblasts including RF and LF (related to collagen deposition) were significantly reduced (Fig.5 E and G), which suggested the different healing outcome subsequently. Although generally the HF formation procedure would not start until several days after wound closure in large wound without implantation (POD14~21) (*3*). In ST profiling of ECM_LW group on POD7, we could identify the initial structure of HF composed of Krt28^{+}HFP in neo-epidermis and Twis2^{+} Dermal condensate (Dc) aggregation beneath in dermis (Fig. 4H), which highlighted the early HF formation signature in ECM_LW group at the spatial gene expression level (Fig. 4I). Based on gene enrichment analysis of ST, ECM_LW sample showed the up-regulated gene expression in hair follicle morphogenesis as well as adaptive immune response (Fig. 4C).To explore the scaffold-induced immune microenvironment, we next integrated the marker genes of immune cells (defined in fig. S9~S19) with ST profiling. Spatial plot of each cluster in ST sections were shown in Fig. 4H and 4L. We noticed the obvious aggregation of MAC and T cell surrounding the biomaterial. Notably, we observed the accumulation of tissue resident (innate lymphoid cell) ILC in epithelium as well as granulation tissue preferantially in ECM_LW group. ILCs which co-expressed genes related to adaptive

immune response as well as hair follicle development might be the critical regulators initiating HF formation (Fig. 4L).

Prediction of critical signaling patterns between spatially colocalized cell populations around biomaterial

Based on the multimodal profiling, we still observed the overlapping distribution of adaptive with the HF precursor cells in ECM_LW group, which implied the potential cellular communication among them. Next, we also applied CellChat to predict the cell-cell communication patterns between EMC_LW and Ctrl_LW (Fig. 5 A and B). The heatmap showed the overall signaling strength of ligand-receptors in Ctrl_LW and ECM_LW group (Fig. 5C). Adaptive immune system related pathways including MHC-II was further activated in ECM_LW. In addition to IL6, the key signaling in embryonic HF development such as FGF(*23*), Notch(*24*), KIT (*19*) were up-regulated in ECM_LW group too. Confirmed in ST profiles, adaptive immune cell and HF precursor cell were enriched for interacting receptor /ligand gene partners including Areg-(Egfr+Erbb2), Epgn- Egfr, Mdk-(Sdc1 or Itgb1), Ptn-(Itgb1or Sdc1) (Fig.5 D and E). The critical functions of epidermal growth factor (EGF)(*25*) , pleiotrophin (PTN) and midkine (MK) (*19*) in skin morphologies has been stressed. Based on our analysis, the adaptive immune cell might modulate the HF precursor cell growth through those pathways, and thus facilitate the HF formation. To testify the role of adaptive immune systems in HF regeneration , we placed ECM scaffolds in the dorsal skin large wound in immunodeficient C57Bl/6 (B6.129-Rag2tm1) mice, which lacked mature T lymphocytes and macrophages (Fig. 5 F and G). We noticed wound closure rate was delayed in Rag2$^{-/-}$ mice (Fig. 5 H~J), and regeneration of HF was scarce in Rag2−/− mice (Fig. 5K). Compared to WT mice which recruited the Cd3+ T cell, we observed the obvious aggregation of Ly6g+ neutrophils around biomaterials in Rag2−/− mice instead. It was necessary to elucidate the underlying mechanisms of mature T cells regulating the homeostasis of neutrophil further.

Biomaterials facilitated the de novo HF regeneration despite of wound size

To detect if there still any difference in wound healing between small or large wound treated with biomaterial, we next repeated small (diameter=0.6cm) and large (diameter=1.5cm) full-thickness wound implanted with biomaterials (Fig.6 A and B). Consistent with ECM_LW group, the scaffold implanted in small wound did not trigger an obvious FBR fibrous capsule either and also owned a rapid degradation rate in small wound (Fig.6 C and D). Histological sections of the ECM_SW tissue still revealed clear signs of enhanced WIHN (Fig.6 C and F). Based on bulk-seq

profiling, heatmaps showed insignificant changes of gene expression HF-related, adaptive immune response, or innate immune response between 2 groups(Fig. S11G). IHC staining for Cd3 and Cd68 confirmed the resembling infiltration level of T cell and macrophage surrounding the scaffold or in granulation tissue (Fig. 6 E). We further explored the differences in immune cell composition using scRNA-seq and ST. The total proportion of macrophage was equilibrium between two groups, and the integrated analysis of ST profiling showed the similar distributions of three subsets around the scaffold (Fig. 6 G and H). Integrated analysis confirmed the substantial distribution of T cell subsets surrounding the scaffold in both groups (Fig. 6 I and J). In summary, the biomaterial showed similar "pro-regenerative" effect on would healing despite of wound size. Besides, this resembling immune-regulatory effect on adaptive immune system indicating the significant role of modulating immune environment in HF regeneration.

Discussion

Problems including delayed would closure, susceptibility to infection, and inability of regenerating appendages have become the main impediment for skin wound healing(*26*). Requirements for the ability to promote nascent HF formation bring significant challenges to biomaterial design, particularly for large-scale full-thickness wound. WIHN is a rare model of mammalian organ regeneration in adult mice wherein large full-thickness wound (>1cm^2) induce few nascent HF regeneration limited in wound center(*3*). The initiation of HF morphogenesis begins when the HFP(*16*) and HFSC(*8*) migrating with neo-epithelium and induced the aggregation of Dc (derived from PF) under them(*27*). The pro-regenerative influence of the immune system in coordinating the early stage of wound repairing has been stressed(*28*). However, the cellular interplay between specific immune subclusters and HF precursor cells remains unclear. Here, we firstly compared the transcriptomics profiles between total "scarring" (Ctrl_SW, diameter = 0.6cm) and "half-regenerative" WIHN (Ctrl_LW, diameter = 1.5cm) model. From our multimodal analysis, we firstly observed the higher proportion of adaptive immune cell from WIHN group (Fig. 2 G and I), which resided in large wound center co-localizing with HF precursor cells (Fig. 2 F and H). The active regional cell-cell communications among them indicated the "pro-regenerative" role of adaptive immune cells in promoting HF neogenesis and served as a promising therapeutic target for the application of immune-regulatory materials in skin wound regeneration (fig. S7). Next, we employed the ECM scaffold for large area skin defect along with the investigation of its role in wound healing and immune microenvironment modulation. The scaffold showed the impact on accelerating wound closure

and promoting the nascent HF formation (Fig. 3 E and H). It was shown that the biomaterial owned a regulatory impact on adaptive immune system. We identified the substantial T cell infiltration in response to scaffold implantation was driven toward regenerative subpopulations, overlapping with the abundant PF (HF-related) (Fig. 5 E, H, and I). The local intercellular communications among the enlarged "pro-regenerative" immune niche and HF precursor cells supported the essential role of adaptive system in HF regeneration mediated by biomaterials (Fig. 6 D and E). Meanwhile, the mild FBR around the scaffold decreased the risk of immune rejection, and the appropriate degrading rate could also avoid the extra expense of secondary surgery. In this study, we firstly defined the spatial heterogeneity of single cell during wound regeneration process mediated by biomaterials. These approaches provided unique media through which we could have a further understanding of delicate immune-regulatory mechanism of biomaterials. Taken together, this study offered an available manner to regenerate skin appendages in severe damage through modulating the adaptive immune system and bring further thoughts in the future design of targeted immune-regulatory materials in scar-less wound regeneration.

References and Notes

1. D. Henn *et al.*, Xenogeneic skin transplantation promotes angiogenesis and tissue regeneration through activated Trem2(+) macrophages. *Science advances* **7**, eabi4528 (2021).doi:10.1126/sciadv.abi4528
2. M. Kurita *et al.*, In vivo reprogramming of wound-resident cells generates skin epithelial tissue. *Nature* **561**, 243-247 (2018).doi:10.1038/s41586-018-0477-4
3. M. Ito *et al.*, Wnt-dependent de novo hair follicle regeneration in adult mouse skin after wounding. *Nature* **447**, 316-320 (2007).doi:10.1038/nature05766
4. M. V. Plikus *et al.*, Regeneration of fat cells from myofibroblasts during wound healing. *Science (New York, N.Y.)* **355**, 748-752 (2017).doi:10.1126/science.aai8792
5. I. C. Boothby, J. N. Cohen, M. D. Rosenblum, Regulatory T cells in skin injury: At the crossroads of tolerance and tissue repair. *Science immunology* **5**, (2020).doi:10.1126/sciimmunol.aaz9631
6. B. A. Shook *et al.*, Myofibroblast proliferation and heterogeneity are supported by macrophages during skin repair. *Science (New York, N.Y.)* **362**, (2018).doi:10.1126/science.aar2971
7. D. Gay *et al.*, Phagocytosis of Wnt inhibitor SFRP4 by late wound macrophages drives chronic Wnt activity for fibrotic skin healing. *Science advances* **6**, eaay3704 (2020).doi:10.1126/sciadv.aay3704
8. X. Wang *et al.*, Macrophages induce AKT/β-catenin-dependent Lgr5(+) stem cell activation and hair follicle regeneration through TNF. *Nature communications* **8**, 14091 (2017).doi:10.1038/ncomms14091
9. D. Gay *et al.*, Fgf9 from dermal γδ T cells induces hair follicle neogenesis after wounding. *Nature medicine* **19**, 916-923 (2013).doi:10.1038/nm.3181

10. A. M. Nelson *et al.*, Interleukin-6 Null Mice Paradoxically Display Increased STAT3 Activity and Wound-Induced Hair Neogenesis. *The Journal of investigative dermatology* **136**, 1051-1053 (2016).doi:10.1016/j.jid.2015.12.043
11. P. Lee *et al.*, Stimulation of hair follicle stem cell proliferation through an IL-1 dependent activation of γδT-cells. *eLife* **6**, (2017).doi:10.7554/eLife.28875
12. B. Yi, Q. Xu, W. Liu, An overview of substrate stiffness guided cellular response and its applications in tissue regeneration. *Bioactive materials* **15**, 82-102 (2022).doi:10.1016/j.bioactmat.2021.12.005
13. K. Sadtler *et al.*, Design, clinical translation and immunological response of biomaterials in regenerative medicine. *Nature Reviews Materials* **1**, 16040 (2016).doi:10.1038/natrevmats.2016.40
14. C. Hu *et al.*, Dissecting the microenvironment around biosynthetic scaffolds in murine skin wound healing. *Science advances* **7**, (2021).doi:10.1126/sciadv.abf0787
15. C. Wang *et al.*, The diameter factor of aligned membranes facilitates wound healing by promoting epithelialization in an immune way. *Bioactive materials* **11**, 206-217 (2022).doi:10.1016/j.bioactmat.2021.09.022
16. M. W. Hughes *et al.*, Msx2 Supports Epidermal Competency during Wound-Induced Hair Follicle Neogenesis. *The Journal of investigative dermatology* **138**, 2041-2050 (2018).doi:10.1016/j.jid.2018.02.043
17. S. Abbasi *et al.*, Distinct Regulatory Programs Control the Latent Regenerative Potential of Dermal Fibroblasts during Wound Healing. *Cell stem cell* **27**, 396-412.e396 (2020).doi:10.1016/j.stem.2020.07.008
18. S. B. Telerman *et al.*, Dermal Blimp1 Acts Downstream of Epidermal TGFβ and Wnt/β-Catenin to Regulate Hair Follicle Formation and Growth. *The Journal of investigative dermatology* **137**, 2270-2281 (2017).doi:10.1016/j.jid.2017.06.015
19. S. Jin *et al.*, Inference and analysis of cell-cell communication using CellChat. *Nature communications* **12**, 1088 (2021).doi:10.1038/s41467-021-21246-9
20. W. Wang *et al.*, Changes in regeneration-responsive enhancers shape regenerative capacities in vertebrates. *Science (New York, N.Y.)* **369**, (2020).doi:10.1126/science.aaz3090
21. C. Seo, M. Kwack, M. Kim, J. Kim, Y. Sung, Activin A-induced signalling controls hair follicle neogenesis. *Experimental dermatology* **26**, 108-115 (2017).doi:10.1111/exd.13234
22. M. Monavarian, S. Kader, S. Moeinzadeh, E. Jabbari, Regenerative Scar-Free Skin Wound Healing. *Tissue engineering. Part B, Reviews* **25**, 294-311 (2019).doi:10.1089/ten.TEB.2018.0350
23. K. Mok *et al.*, Dermal Condensate Niche Fate Specification Occurs Prior to Formation and Is Placode Progenitor Dependent. *Developmental cell* **48**, 32-48.e35 (2019).doi:10.1016/j.devcel.2018.11.034
24. N. Ali *et al.*, Regulatory T Cells in Skin Facilitate Epithelial Stem Cell Differentiation. *Cell* **169**, 1119-1129.e1111 (2017).doi:10.1016/j.cell.2017.05.002
25. A. Nosbaum *et al.*, Cutting Edge: Regulatory T Cells Facilitate Cutaneous Wound Healing. *Journal of immunology (Baltimore, Md. : 1950)* **196**, 2010-2014 (2016).doi:10.4049/jimmunol.1502139
26. S. Mascharak *et al.*, Preventing Engrailed-1 activation in fibroblasts yields wound regeneration without scarring. *Science (New York, N.Y.)* **372**, (2021).doi:10.1126/science.aba2374

27. V. Thulabandu, D. Chen, R. P. Atit, Dermal fibroblast in cutaneous development and healing. *Wiley interdisciplinary reviews. Developmental biology* **7**, (2018).doi:10.1002/wdev.307
28. G. Wang *et al.*, Bacteria induce skin regeneration via IL-1β signaling. *Cell host & microbe* **29**, 777-791.e776 (2021).doi:10.1016/j.chom.2021.03.003

Acknowledgments: We thank the Novogene company for RNA sequencing work, and the National Clinical Research Center for Oral Diseases & State Key Laboratory of Oral Diseases for animal experiment, and the Analytical & Testing Center of Sichuan University for the fabrication of biomaterials. We thank Jia-yu Gao and Sheng-an Rung for the help with analysis.

Funding: Sichuan Science and Technology Plan grant 2022YFS0041 (Y.L.Q.)

Interdisciplinary Innovation Project, West China Hospital of Stomatology Sichuan University grant RD-03- 202006 (Y.M.)

Research and Develop Program, West China Hospital of Stomatology Sichuan University grant LCYJ2019-19 (Y.M.)

Author contributions:

Conceptualization: YY, CYC

Methodology: CYC, LL, CH, CBW

Investigation: YY, XHL

Visualization: YY

Writing – original draft: YY

Writing – review & editing: CCY

Funding acquisition & Project administration & Supervision: YM, YLQ, CCY

Competing interests: Authors declare that they have no competing interests.

Data and materials availability: All data to support the conclusions in this manuscript can be found in the figures and the supplementary materials. Any other data can be requested from the corresponding authors.

Supplementary Materials

Materials and Methods

Supplementary Text

Figs. S1 to S12

References (*39–##*)

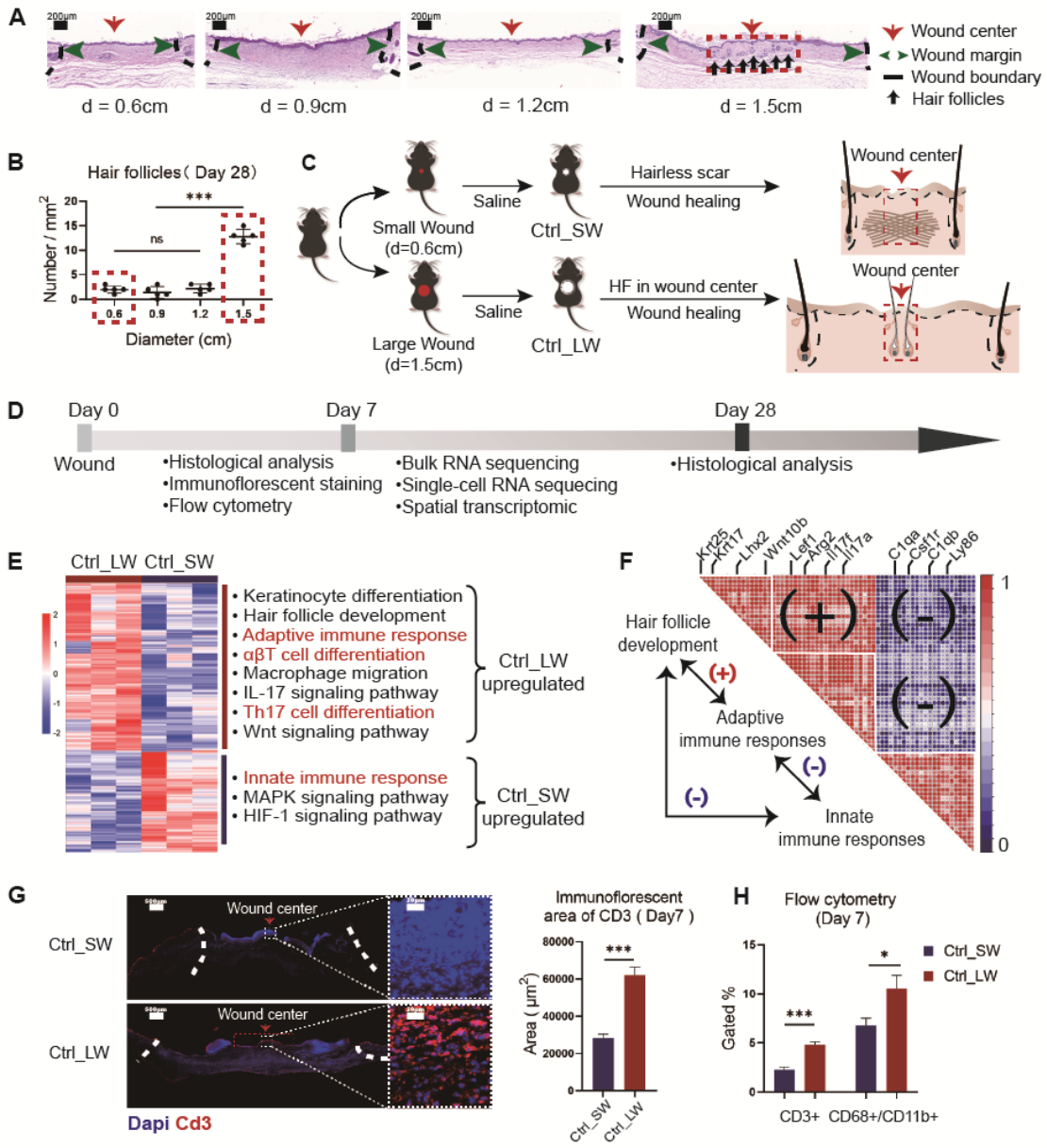

Fig. 1. Evaluation of the healing of small and large full-thickness wound. (A) Haematoxylin and eosin (H&E) staining evaluating skin wound healing outcomes of different wound size. (B) Histologic quantification of de novo hair follicles. (C) Surgical process for the mice full-thickness excisional splinted of small (Ctrl_SW) and large (Ctrl_LW) wound and different healing outcomes. (D) Workflow for evaluating mice skin wound healing of different wound size. (E) Heatmap showing hierarchical clustering of differentially expressed genes (p value<0.05 & |log2FC|> 1) , and gene set enrichment analysis showing the up-regulated GO terms and KEGG pathways between two groups. (F) Pearson correlation analysis shows relation

between the gene expression of hair follicle development related genes, adaptive immune responses related genes and innate immune responses related genes (positive, red; negative, blue). (G) IF staining of Cd3 (red) in histologic sections and corresponding quantification. (H) In vivo flow cytometry strategy using Cd3 to identify T cells; monocyte, and macrophages co-expressing the surface markers CD68 and CD11b, and the corresponding quantification.

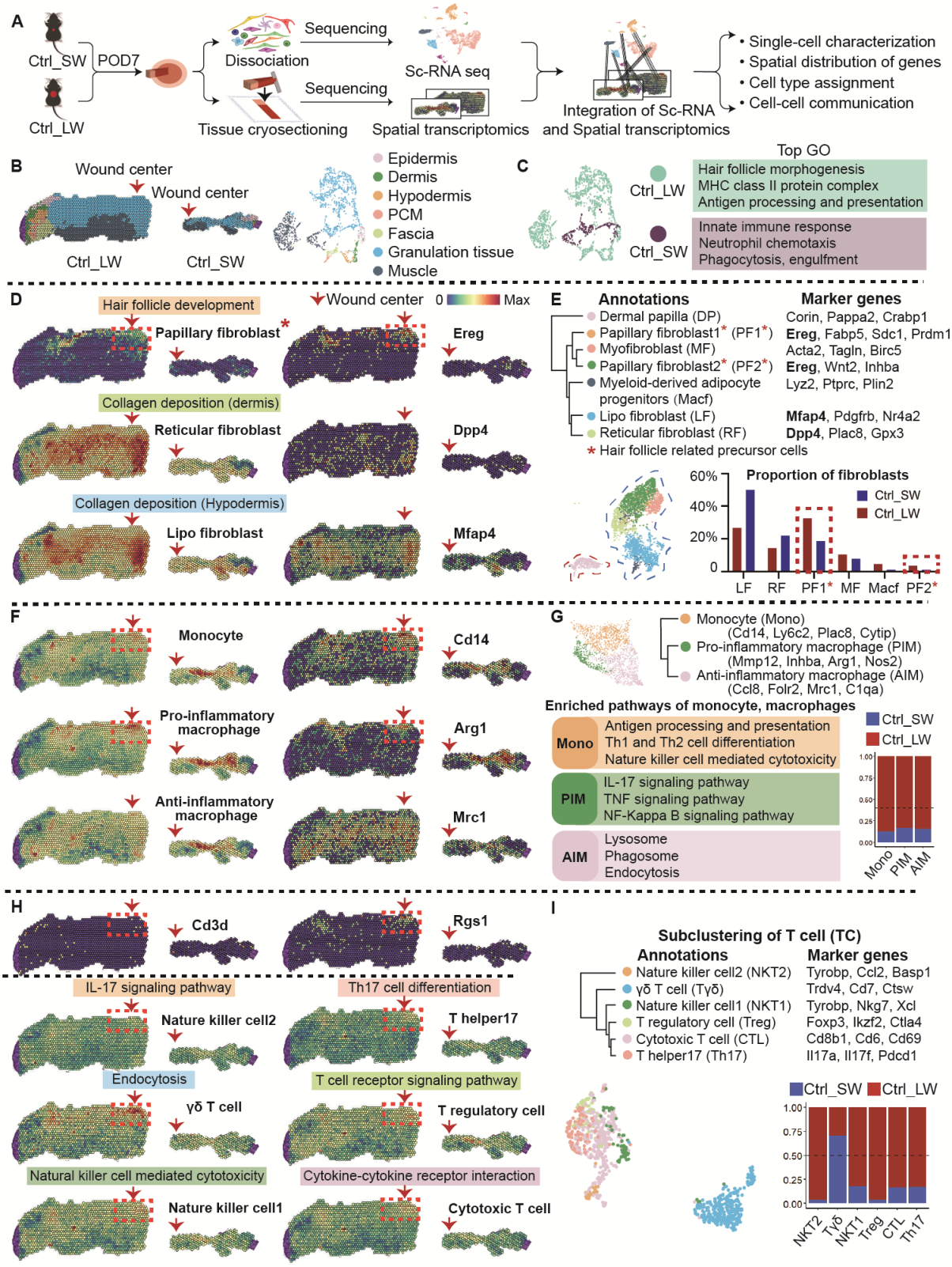

Fig. 2. Spatial transcriptomics applied to Ctrl_SW and Ctrl_LW. (A) Schematic for

generating sc-RNA seq and spatial transcriptomics data from splinted excisional wounds. (B) Spatial plots and UMAP plot showing that the anatomical regions could be distinguished by their transcriptional programs. (C) Gene enrichment analysis between Ctrl_SW and Ctrl_LW. (D) Spatial feature plots showed defined fibroblast subclusters distribution in tissue sections. (E) Subclustering of fibroblast in sc-RNA seq dataset. (F) Spatial feature plots showed defined MAC subclusters distribution in tissue sections. (G) Subclustering of monocyte, macrophages (MAC) in sc-RNA seq dataset (H) Spatial feature plots showed expression of Cd3d and Rgs1 (marker genes of TC) and defined TC subclusters distribution in tissue sections. (H) Subclustering of T cells (TC) in Sc-RNA seq dataset.

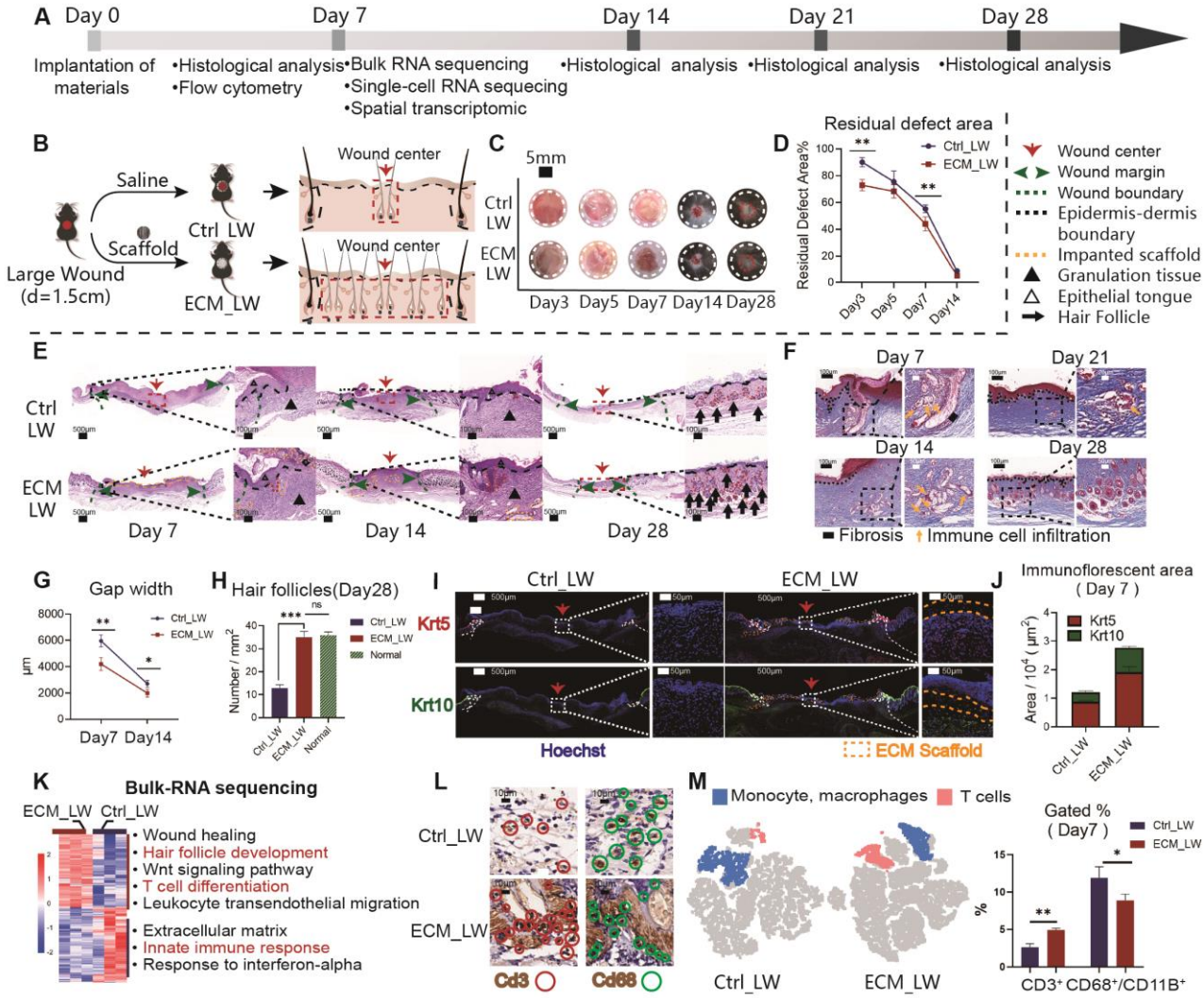

Fig. 3. Evaluation of the healing of large full-thickness wounds with/without implanted ECM scaffolds. (A) Workflow for evaluating large-scale wound healing. (B) Surgical processes for skin excisional wound model. (C) Residual wound area at 3, 5, 7, 14 and 28 days, and (D) corresponding analysis. (E) H&E analysis of two groups. (F) Evaluation of FBR around the biomaterials. Masson's trichrome staining for ECM_LW group on POD 7, 14, 21 and 28. (G) Semiquantitative evaluation of gap width. (H) Histologic quantification of de novo HFs on POD28. (I) IF staining using Krt5 (red) and Krt10 (green) and (J) semiquantitative evaluation of the fluorescent area. (K) Heatmap showing hierarchical clustering of differentially expressed genes (p value<0.05 & |log2FC|> 1) and gene set enrichment analysis. (L) IHC staining of Cd3 and Cd68. (H) In vivo flow cytometry strategy using Cd3 to identify T cells; monocyte, and

macrophages co-expressing the surface markers CD68 and CD11b, and the corresponding quantification.

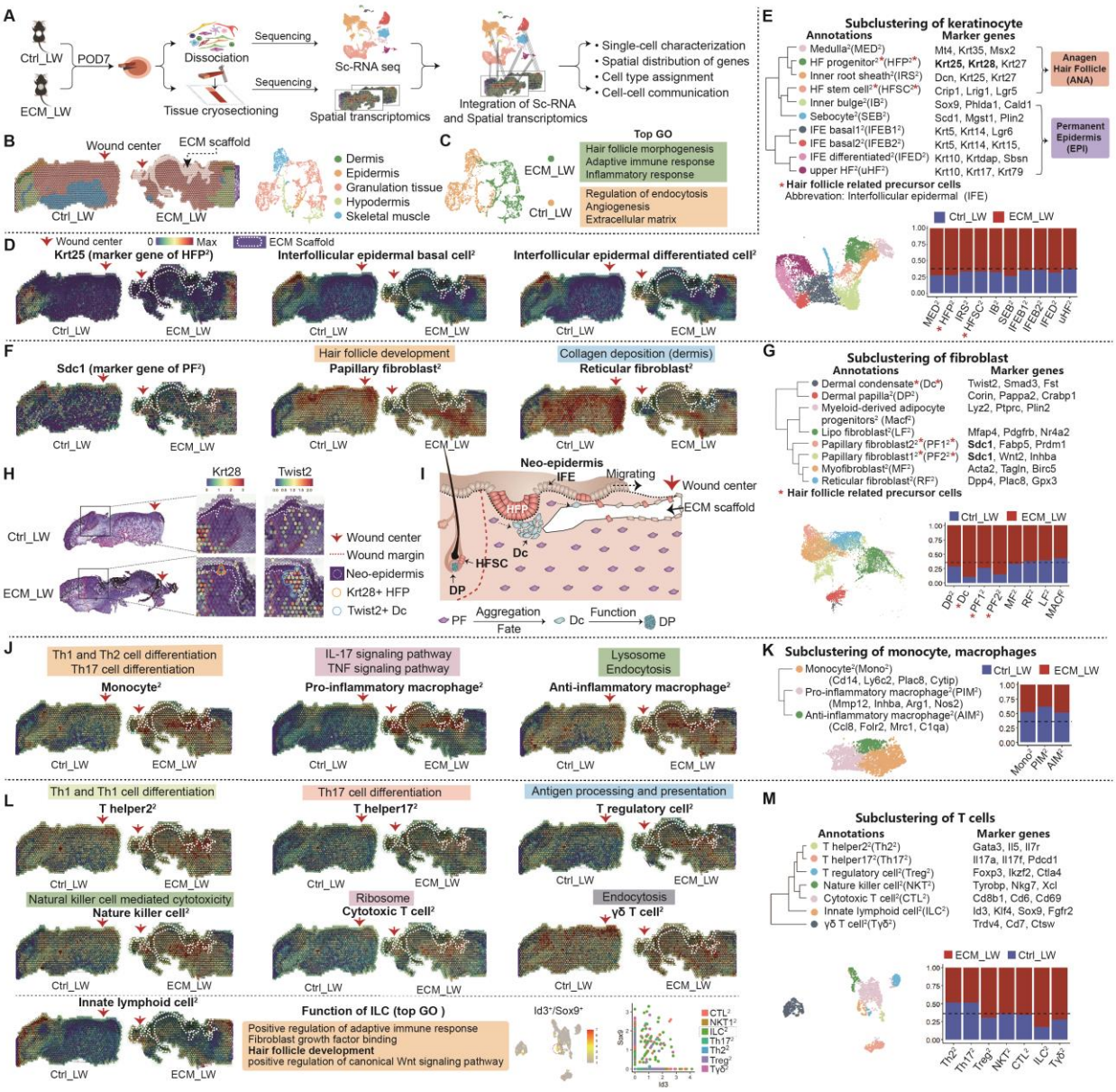

Fig. 4. Spatial transcriptomics applied to ECM_LW and Ctrl_LW. (A) Schematic for generating scRNA-seq and spatial transcriptomics data from splinted excisional wounds. (B) The unsupervised clustering indicated the anatomical structure of sample. (C) Gene enrichment analysis between ECM_LW and Ctrl_LW. (D) Spatial feature plot showed the expression of Krt25 (marker gene for hair follicle progenitor) and defined keratinocyte subclusters (related to Fig.S9) in tissue sections. (E) Subclustering of keratinocyte in sc-RNA seq dataset. (F) Spatial feature plot showed the expression of Sdc1 (marker gene for papillary fibroblast) and defined fibroblast subclusters (related to Fig.S9) in tissue sections. (G) Subclustering of fibroblast in sc-RNA seq dataset. (H) Spatial feature plot highlighted the expression of Krt28+ Hair follicle

progenitor and Twist2+ Dermal condensate in migrating neo-epidermis. (I) Illustration showed the epithelialization along with de novo HF formation in ECM_LW group. (J) Spatial feature plot showed the expression of defined monocyte, macrophage (MAC) subclusters (related to Fig.S10) in tissue sections. (E) Subclustering of MAC in sc-RNA seq dataset. (L) Spatial feature plot showed the expression of defined T cell subclusters (related to Fig.S10) in tissue sections. (M) Subclustering of T cell in sc-RNA seq dataset.

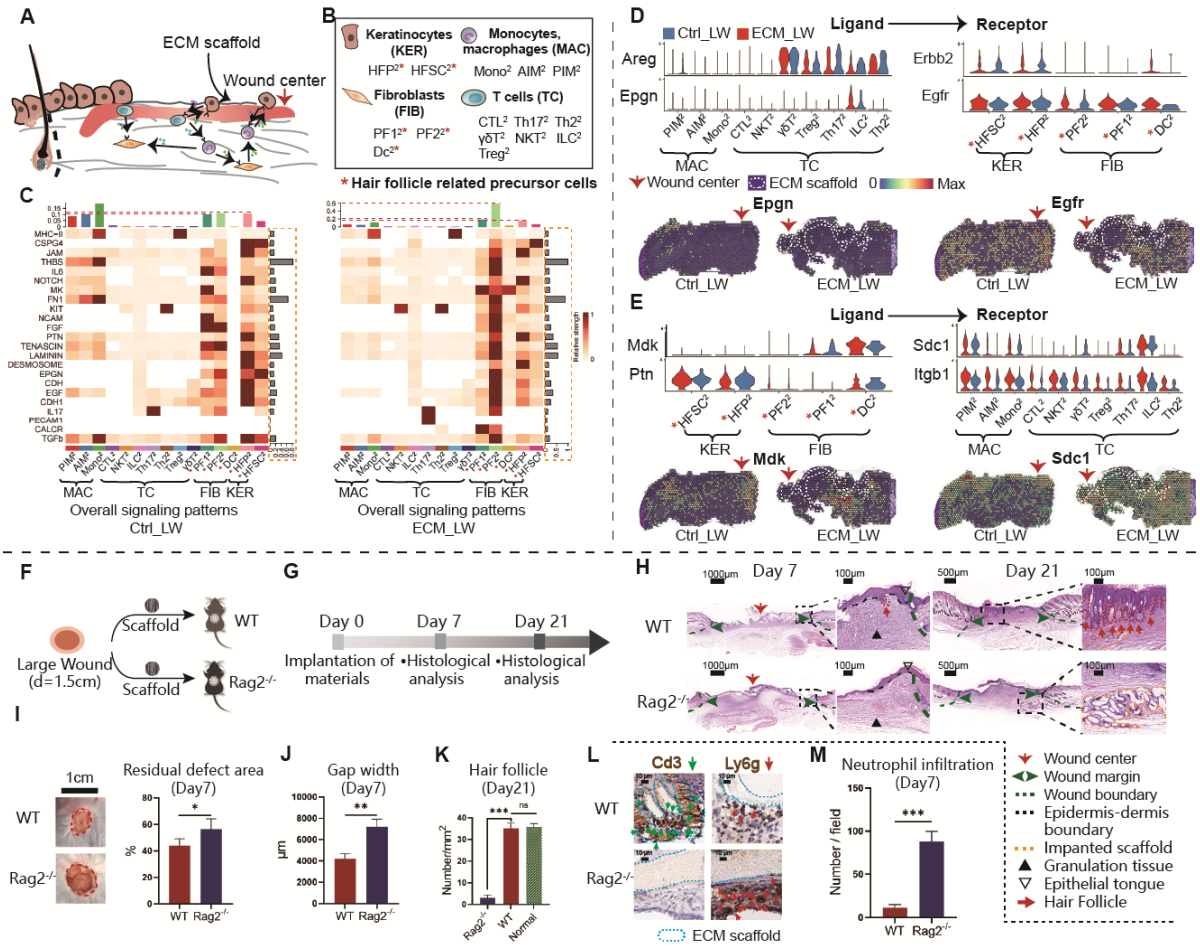

Fig. 5. Cellular communication landscape between immune cells and cutaneous cells in ECM_LW and Ctrl_LW group. (A) Schematic of combined ligand-receptor analysis between cutaneous cells and adaptive immune cells . (B) Defined subclusters in corresponding scRNA-seq dataset. (C) Comparison of overall cell-cell communication patterns between Ctrl_LW and ECM_LW using CellChat. (D and E) Violin plot (scRNA-seq) and spatial feature plots (ST) showed select ligands and cognate receptor expression. (F) Surgical process and (G) workflow for evaluating large area wound healing mediated by ECM scaffold in Rag2$^{-/-}$ and WT mice. (H) Residual defect area at 7 days after wound. (I) Histological analysis of wound healing in WT and Rag2$^{-/-}$ mice. (J) Semiquantitative evaluation of gap width. (K) Histologic quantification of de novo HFs. (L) IHC staining of Cd3 and Ly6g. (M) Quantification of Ly6g+ neutrophil infiltration.

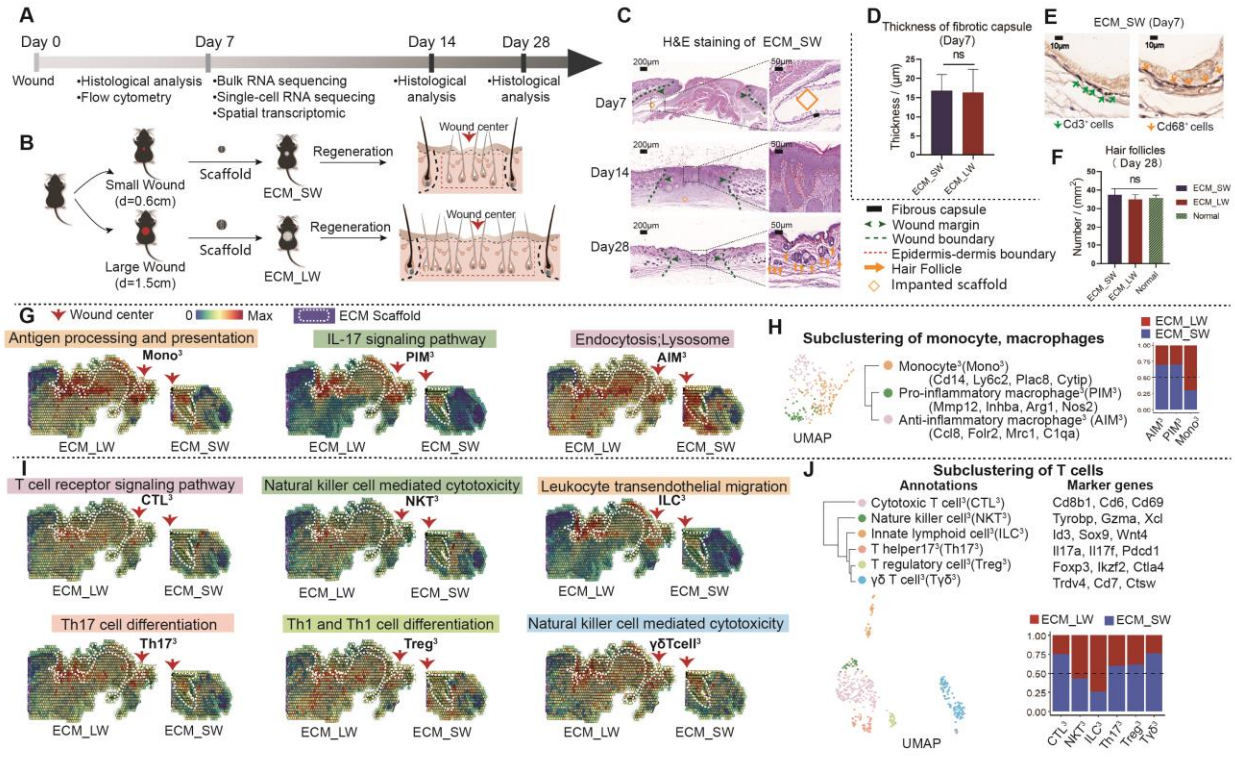

Fig. 6. Evaluation of the healing of small and large full-thickness wound with implanted ECM scaffolds. (A) Workflow for evaluating skin wound healing. (B) Surgical process for skin excisional wound model of ECM_SW and ECM_LW group. (C) H&E staining of ECM_SW samples. (D) Thickness of fibrotic capsule around membrane of ECM_SW and ECM_LW group. (E) IHC staining of Cd3 and Cd68. (F) Histologic quantification of de novo hair follicles on POD28. (G) Spatial feature plot showed the expression of defined monocyte, macrophage (MAC) subclusters (related to Fig.S10) in tissue sections. (H) Subclustering of MAC in sc-RNA seq dataset. (I) Spatial feature plot showed the expression of defined T cell subclusters (related to Fig.S10) in tissue sections. (J) Subclustering of T cell in sc-RNA seq dataset.